

# The Human Skin Barrier Is Organized as Stacked Bilayers of Fully Extended Ceramides with Cholesterol Molecules Associated with the Ceramide Sphingoid Moiety

Ichiro Iwai<sup>1,2</sup>, HongMei Han<sup>1,8</sup>, Lianne den Hollander<sup>1,8</sup>, Stina Svensson<sup>1,3</sup>, Lars-Göran Öfverstedt<sup>4</sup>, Jamshed Anwar<sup>5</sup>, Jonathan Brewer<sup>6</sup>, Maria Bloksgaard<sup>6</sup>, Aurelie Laloeuf<sup>1</sup>, Daniel Nosek<sup>1,7</sup>, Sergej Masich<sup>1</sup>, Luis A. Bagatolli<sup>6</sup>, Ulf Skoglund<sup>4</sup> and Lars Norlén<sup>1,7</sup>

The skin barrier is fundamental to terrestrial life and its evolution; it upholds homeostasis and protects against the environment. Skin barrier capacity is controlled by lipids that fill the extracellular space of the skin's surface layer—the stratum corneum. Here we report on the determination of the molecular organization of the skin's lipid matrix *in situ*, in its near-native state, using a methodological approach combining very high magnification cryo-electron microscopy (EM) of vitreous skin section defocus series, molecular modeling, and EM simulation. The lipids are organized in an arrangement not previously described in a biological system—stacked bilayers of fully extended ceramides (CERs) with cholesterol molecules associated with the CER sphingoid moiety. This arrangement rationalizes the skin's low permeability toward water and toward hydrophilic and lipophilic substances, as well as the skin barrier's robustness toward hydration and dehydration, environmental temperature and pressure changes, stretching, compression, bending, and shearing.

*Journal of Investigative Dermatology* (2012) **132**, 2215–2225; doi:10.1038/jid.2012.43; published online 26 April 2012

## INTRODUCTION

The skin constitutes a barrier between the body and the environment (Elias and Friend, 1975). By preventing water loss via evaporation it upholds homeostasis, and by preventing penetration of exogenous substances it protects against the environment. The skin's barrier capacity is a function of the molecular architecture of the lipid structure in the extracellular space between the cells of the stratum corneum (Bouwstra *et al.*, 1991). The lipids consist of a heterogeneous

mixture of saturated, long-chain ceramides (CERs), free fatty acids (FFAs), and cholesterol (CHOL) in a roughly 1:1:1 molar ratio (Wertz and Norlén, 2003). In the CER fraction alone, more than 300 different species have been identified (Masukawa *et al.*, 2009).

Ever since the discovery in the early 1970s (Breathnach *et al.*, 1973; Elias and Friend, 1975) that the stratum corneum extracellular space is filled with lipid material, the skin lipids have been a subject of much activity. However, the molecular organization of these lipids remains unresolved. By using conventional electron microscopy (EM) on ruthenium tetroxide-stained mouse skin, Madison *et al.* (1987) reported that the stratum corneum lipid material, or "lipid matrix", displays 13-nm repeating units of broad:narrow:broad electron lucent bands. Using small-angle X-ray diffraction on isolated human stratum corneum, Garson *et al.* (1991) reported the presence of one 4.5-nm and one 6.5-nm diffraction peak related to lipids. Concomitantly, White *et al.* (1988) and Bouwstra *et al.* (1991) reported the presence of a 13-nm repeating unit in mouse and human isolated stratum corneum, respectively. Later, McIntosh (2003) observed an asymmetric distribution of CHOL within model systems composed of reconstituted stratum corneum lipids extracted from pig skin. On the basis of these data, as well as on data obtained from different *in vitro* lipid model systems, six theoretical models for the molecular arrangement of the extracellular lipid matrix have been

<sup>1</sup>Department of Cell and Molecular Biology (CMB), Karolinska Institutet, Stockholm, Sweden; <sup>2</sup>Shiseido Research Center, Yokohama, Japan; <sup>3</sup>Center for Image Analysis, Swedish University of Agricultural Sciences, Uppsala, Sweden; <sup>4</sup>Structural Cellular Biology Unit, Okinawa Institute of Science and Technology, Okinawa, Japan; <sup>5</sup>Institute of Pharmaceutical Innovation, University of Bradford, Bradford, United Kingdom; <sup>6</sup>Department of Biochemistry and Molecular Biology, Membrane Biophysics and Biophotonics group/MEMPHYS-Center for Biomembrane Physics, University of Southern Denmark, Odense, Denmark and <sup>7</sup>Dermatology Clinic, Karolinska University Hospital, Stockholm, Sweden

<sup>8</sup>These authors contributed equally to this work.

Correspondence: Lars Norlén, Department of Cellular and Molecular Biology (CMB), Karolinska Institutet, von Euler's v 1, 171 77 Stockholm, Sweden.  
E-mail: lars.norlen@ki.se

Abbreviations: CEMOVIS, cryo-electron microscopy of vitreous skin section; CER, ceramide; CHOL, cholesterol; EM, electron microscopy; FFA, free fatty acid; GP, generalized polarization; LAURDAN, 6-dodecanoyl-2-dimethylaminonaphthalene

Received 12 May 2011; revised 12 December 2011; accepted 17 December 2011; published online 26 April 2012

proposed. These are based on either triple-band repeating units and/or bands with the same width (Supplementary Figure S1 online).

We have used a novel methodological approach based on cryo-electron microscopy of vitreous skin section (CEMOVIS) defocus series combined with molecular modeling and EM simulation to investigate the molecular organization of the human skin's lipid matrix in its near-native state. In CEMOVIS, the native tissue is preserved down to the molecular level, and the micrograph pixel intensity is directly related to the local electron density of the specimen (Dubochet *et al.*, 1988; Al-Amoudi *et al.*, 2004, 2007; Norlén *et al.*, 2009). Biomolecules generally possess small intermolecular and intramolecular differences in electron density, as they are essentially composed of atoms with similar atomic weight (carbon, nitrogen, and oxygen). However, for orderly arranged molecular assemblies, such as lipid tails and headgroups in membranes, even small differences in shape and atomic composition may be amplified because of interference effects that appear in the image phase contrast. During image acquisition, phase contrast is made visible using defocus (compare e.g., Fanelli and Öktem, 2008).

Here we show that the human skin barrier's CEMOVIS pattern is characterized by an asymmetric ~11-nm repeating unit consisting of alternating narrow (~4.5 nm) and broad (~6.5 nm) bands. Further, at, and only at, very high magnification (pixelsize  $\leq 3.31 \text{ \AA}$ ), complex interference patterns can be resolved in the CEMOVIS micrographs. Exploiting this, CEMOVIS micrographs were recorded repeatedly at very high magnification at the same position of the skin sample while increasing stepwise the microscope's defocus, thus ensuring that differences in the recorded micrographs were due exclusively to the different defocuses used. Simulated electron micrographs were then generated at corresponding defocuses for different skin lipid models, and compared with the CEMOVIS micrographs. This approach was found to be highly discriminating between different models.

The lipid organization that emerges from the analysis is a stacked bilayer structure of CERs in the fully extended (splayed chain) conformation with CHOL associated with the CER sphingoid moiety.

## RESULTS

### Skin lipid's CEMOVIS pattern

The CEMOVIS data reported here represent over 1,000 original observations obtained from the left volar forearm and abdomen of five Caucasian men in the age group of 40–50 years with no history of skin disease.

The CEMOVIS data demonstrate that the stratum corneum extracellular lipid matrix is composed of a stack of layers (Figure 1a). They display a meandering pathway (Figure 1a) and folds/unfolds on hydration/dehydration (Supplementary Figure S2A–C online). This implies that these layers are malleable. At high magnification (Figure 1d), the distinct dark lines of the lamellar stacks (Figure 1b) are revealed to be not entirely continuous. There are regular breaks in intensity, implying some disorder at the microstructural level (Figure 1d, white solid arrows; Supplementary Figure S4A online). At these

breaks, the intensity is displaced away from and perpendicular to the mainstream intensity bands, giving rise to thin dark "cross-stripes" (Figure 1d, white open arrows; Supplementary Figure S4A online).

The averaged, image intensity profile for the stacked lipids (Figure 1e) was obtained by fuzzy distance-based image analysis and is shown in Figure 1b and c. Lamellar regions with 2, 4, 6, 8, 10, or 12 dark lines (Figure 2a–f, left column) can be observed between adjacent stratum corneum cell plasma membranes (also referred to as "lipid envelopes"). The dark lines are arranged in a periodic pattern with an asymmetric ~11-nm (10–12 nm) repeating unit consisting of alternating narrow (~4.5 nm) and broad (~6.5 nm) bands, where the 4.5-nm bands express a higher averaged image intensity (i.e., they are darker) than the 6.5-nm bands (Figure 2a–f, right column). A low-intensity region (i.e., a light band) is present in the mid-plane of the 6.5-nm bands (Figure 1b, solid black arrows; Supplementary Figure S4A online). Small "shoulders" centrally on each slope of the corresponding averaged intensity profiles delimit its extension (Supplementary Figure S4B online, open arrows). No interindividual or intersite (forearm vs. abdomen) variation was recorded (Supplementary Figure S5 online).

Power spectra extracted along the lamellar stacks revealed that the 6.5-nm region, around its low-intensity mid-plane, is somewhat ordered, whereas the other regions appear to be unstructured (Figure 3a–g). The 6.5-nm region is characterized by peaks equating to repeat distances of 2.3–3.0 nm and 1.5–1.7 nm (Figure 3d).

Generalized polarization (GP) function measurements obtained from multi-photon excitation images of 6-dodecanoyl-2-dimethylaminonaphthalene (LAURDAN) labeled near-native skin (Figure 4a and b) show that the stratum corneum lipid matrix is in a condensed state and contains little, if any, water at the lipid headgroup/hydrocarbon interface regions. Furthermore, the LAURDAN GP function was not affected by hydration (Figure 4a and b). Similarly, the CEMOVIS intensity profiles of the extracellular lipid matrix remained unaltered upon hydration (Figure 4c and d), whereas the intracellular keratin intermediate filament network at the same locations swelled extensively (Figure 4c; compare Supplementary Figure S2A online) compared with normal stratum corneum (Figure 1a; compare Supplementary Figure S2B online).

### Modeling and simulation

The key aspect of the lipid matrix' CEMOVIS image intensity profile is the asymmetric ~11-nm repeating unit. This consists of two peaks with a peak-peak distance of ~4.5 nm separated by a shallow trough of low intensity (Figure 2). The twin-peak repeats are separated by a deeper (low intensity) trough with a peak-peak distance of ~6.5 nm. The peaks are expected to correspond to the lipid headgroup regions, which are characterized by the heavier polar atoms nitrogen and oxygen. The low-intensity troughs are expected to correspond to the carbon-dominated lipid alkyl chains.

Given these characteristics of the data, we decided to combine molecular modeling and EM simulation (Figure 5) to identify a lipid organization that would be consistent not only

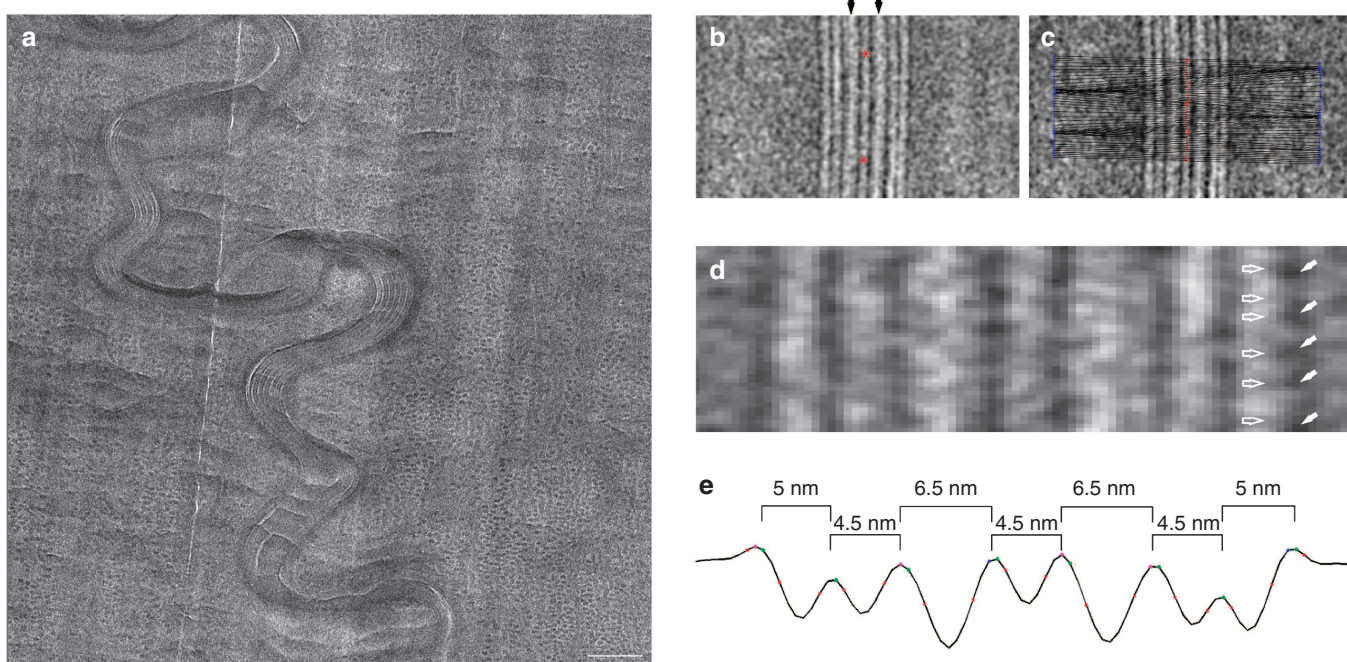


**Figure 1. The cryo-electron microscopy of vitreous skin section (CEMOVIS) intensity pattern of the stratum corneum extracellular lipid matrix consists of folded stacked layers.** (a) Medium-magnification CEMOVIS micrograph of the interface between two cells in the mid-part of the stratum corneum. Note that in CEMOVIS the tissue is unstained, and that the pixel intensity is directly related to the local electron density of the sample. The stacked lamellar pattern represents the extracellular lipid matrix. Dark ~10-nm dots represent keratin intermediate filaments filling out the intracellular space. Note that the extracellular lipid matrix locally expresses extensive folding. (b) High-magnification CEMOVIS micrograph of the extracellular space in the mid-part of the stratum corneum. The intensity profile of the lipid matrix was obtained by fuzzy distance-based image analysis. The red stars in (b) represent the manually chosen start and end points for fuzzy distance-based path growing. (c) The red line represents the traced-out path. Stacked lines mark extracted intensity profiles. (d) Enlarged area of the central part of (b). Note that the electron-dense bands are composed of dark 1- to 3-nm dots from which thin, weak lines protrude 2–3 nm into the lucent areas. The same pattern is also evident in (b). (e) Reversed averaged pixel intensity profile obtained from the extracted area in (c). Peaks in (e) correspond to dark bands and valleys to lucent bands in (d). Black arrows in (b) denote electron lucent narrow bands at the center of the 6.5-nm bands. Section thickness: ~50 nm (a–d). Bar (a): 100 nm. Pixel size in (a–d): 6.02 Å.

with the observed intensity profile but also with the CEMOVIS intensity interference pattern changes observed on changing the microscope's defocus during image acquisition (Figure 6).

Rather than considering the full complexity of the stratum corneum lipid composition, we focused on the three main components (Wertz and Norlén, 2003; Masukawa *et al.*, 2009), namely CER NP (C18-phytosphingosine-non-hydroxy-C24:0), CHOL, and lignoceric acid (C24:0), because these will likely determine the main features of the lipid organization, and variation in chain lengths will serve only to modulate the structure. Polyunsaturated  $\omega$ -hydroxyacid CERs were not included, as these correspond to <15% of the total lipid mass extracted from the stratum corneum and are structurally different from the remaining stratum corneum lipids.

Further, water was not included in the models as neither the LAURDAN GP (Figure 4a and b) nor the CEMOVIS (Figure 4c and d) swelling experiments expressed signs of the presence of water in the lipid matrix.

For each of the three lipid components, we built molecular models with the atoms located at their ideal bond distances, angle, and torsions. The torsions in the headgroup region of the CER molecules were chosen to yield either a fully extended

(the splayed chain conformation; compare Supplementary Figures S6–S7 online) or a fully folded (the hairpin conformation; compare Supplementary Figure S8 online) structure.

EM image intensity patterns were then simulated for a variety of molecular models at three radically different defocuses ( $-0.5$ ,  $-2$ , and  $-5$   $\mu\text{m}$ ; Figure 6d–f; Supplementary Figures S6–S8 online) using a newly developed EM simulator (Rullgård *et al.*, 2011). The different stratum corneum lipid models were thus discriminated by how closely their corresponding simulated EM patterns mirrored the CEMOVIS patterns of near-native skin, and how closely they reflected the CEMOVIS interference pattern changes observed upon radically changing the microscope's defocus during image acquisition (Figure 6a–f; Supplementary Figures S6–S8 online). For the best-fitting model (Supplementary Figure S6D online), EM images were simulated at  $-1$ ,  $-2$ , and  $-3$ - $\mu\text{m}$  defocus (Figure 6j–l) and compared with a series of CEMOVIS micrographs obtained sequentially at the same location at  $-1$ ,  $-2$ , and  $-3$ - $\mu\text{m}$  defocus (Figure 6g–i).

Remarkably, of the various molecular organizations considered, a model based on bilayers of fully extended CERs with CHOL selectively localized to the CER sphingoid part was found to account for all the major features of the

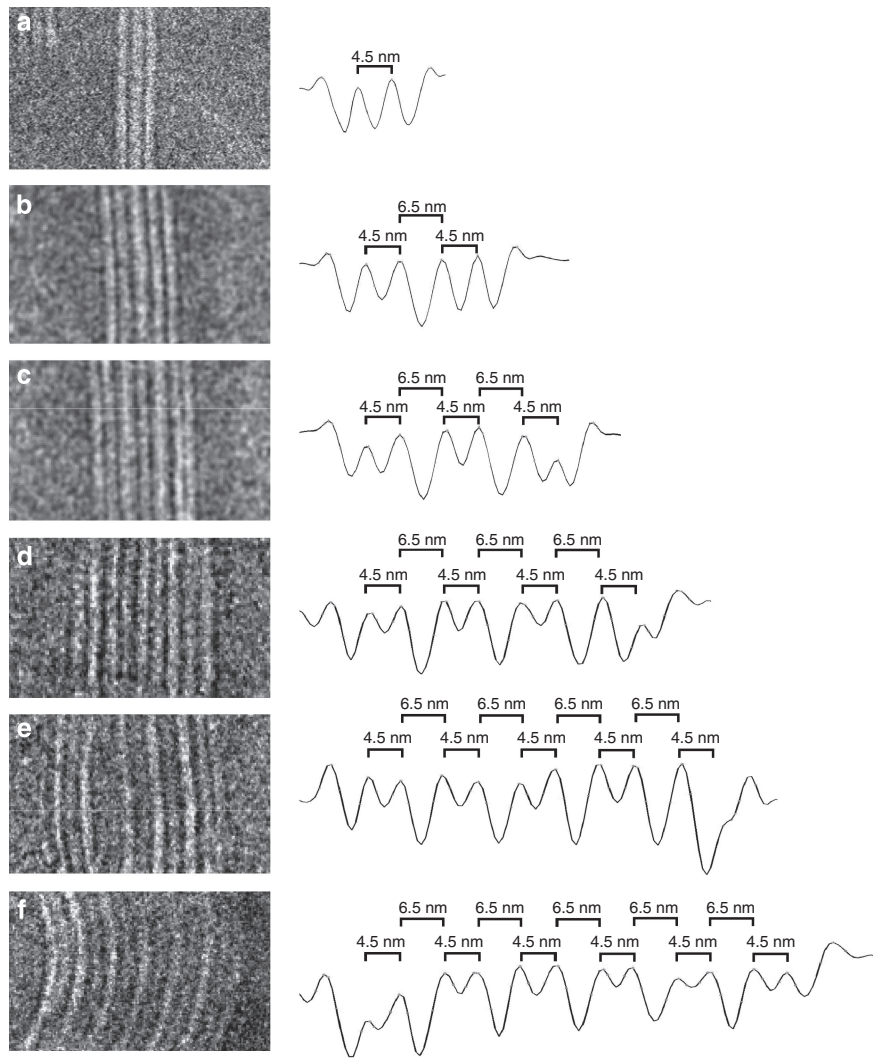


**Figure 2. An asymmetric ~11-nm repeating unit characterizes the cryo-electron microscopy of vitreous skin section (CEMOVIS) intensity profile of the lipid matrix.** Left column: high-magnification CEMOVIS micrographs of the extracellular space in the mid-part of the stratum corneum of vitrified epidermis. Right column: corresponding intensity profiles obtained from fuzzy distance-based image analysis. (a) Two high-intensity (dark) lines between stratum corneum cell borders. (b) Four high-intensity lines. (c) Six high-intensity lines. (d) Eight high-intensity lines. (e) Ten high-intensity lines. (f) Twelve high-intensity lines. Section thickness: ~50 nm (a-f). Pixel size in (a): 3.31 Å, and in (b-f): 6.02 Å.

CEMOVIS images at all defocuses (Figure 6). None of the other lipid models could account for any major feature of the CEMOVIS images at any defocus. For reference and comparison, the simulated electron micrographs for all the lipid models tested are given in Supplementary Figures S6–S8 online. From these simulated images, it is clear that only bilayer models in which the CER molecules are in the fully extended conformation show any similarity to the observed CEMOVIS data (Supplementary Figure S6 online). The folded (hairpin) CER conformation and stacked monolayers of extended CERs are readily discounted (Supplementary Figures S7 and S8 online).

We specifically explored whether the simulated images are sensitive to how CHOL is distributed within the lipid model, given the reported asymmetric distribution of CHOL within model systems composed of reconstituted stratum corneum lipids (McIntosh, 2003). We considered models

(i) without CHOL (Supplementary Figure S6E online), (ii) with CHOL selectively localized to the CER sphingoid part (Supplementary Figure S6D online), (iii) with CHOL selectively localized to the CER fatty acid part (Supplementary Figure S6F online), and (iv) with CHOL homogeneously distributed between the CER fatty acid and sphingoid parts (Supplementary Figure S6G–J online). The simulations reveal that the CEMOVIS patterns are remarkably sensitive to CHOL distribution and suggest that CHOL is selectively localized to the CER sphingoid part (Supplementary Figure S6D online).

## DISCUSSION

The lipid organization that emerges from the analysis is a bilayer structure of fully extended CERs with the sphingoid moieties interfacing. Both CHOL and the FFA appear to be selectively distributed: CHOL at the CER sphingoid end and the FFA at the CER fatty acid end. The characteristic

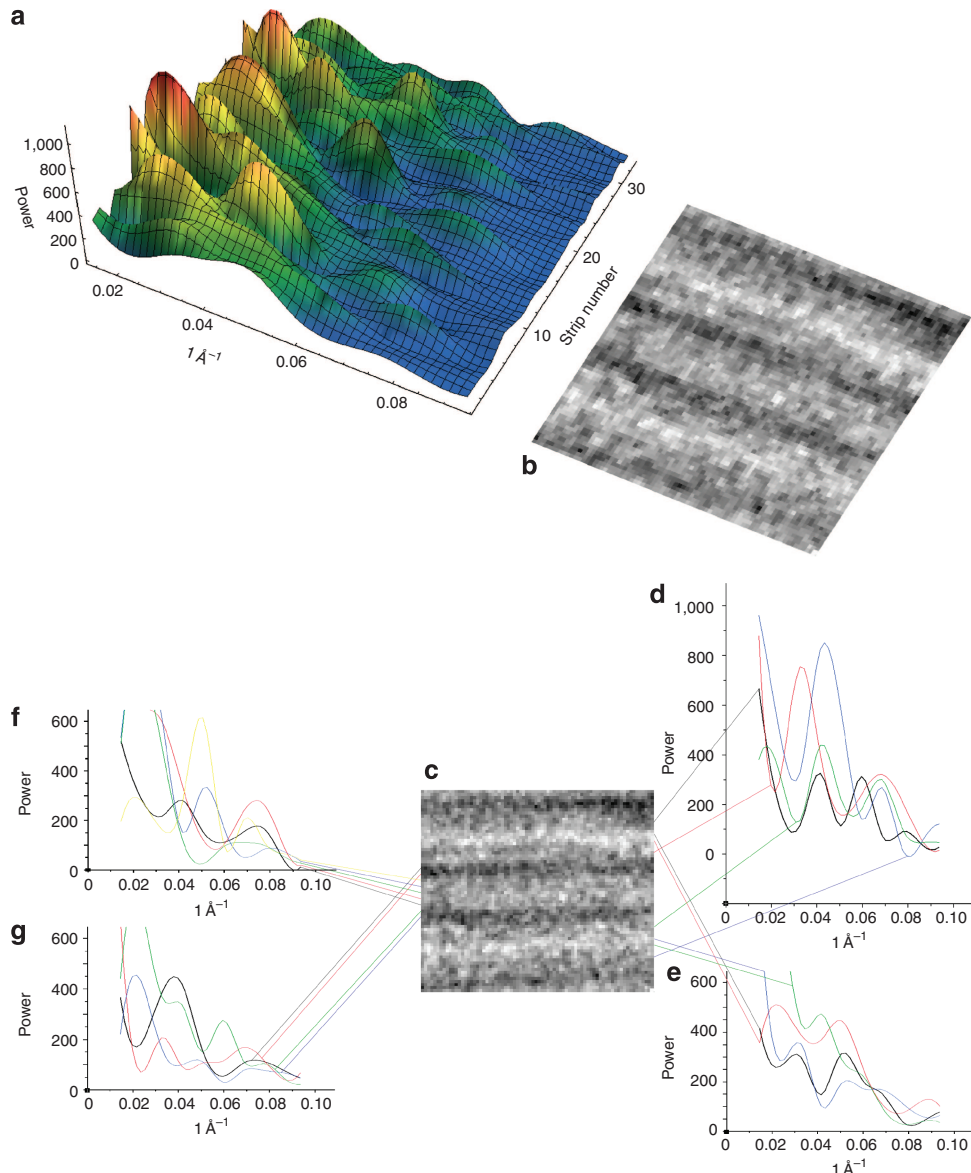


**Figure 3. Cryo-electron microscopy of vitreous skin section (CEMOVIS) micrograph power spectra analysis indicates different molecular packing orders in different regions within the lamellar structure.** (a) Surface plot of all power spectra obtained along the lamellar pattern of a CEMOVIS micrograph (b, c, Figure 5a) of a unit of one central 4.5-nm band with two adjacent 6.5-nm bands. The power spectra of the 6.5-nm bands, besides their mid-plane, show recurring characteristics, represented by one 2.3- to 3.0-nm peak and one 1.5- to 1.7-nm peak (d). The 6.5-nm bands, besides their low-intensity mid-plane, are thus somewhat ordered. The power spectra extracted from the remaining regions are more amorphous with nonreproducible characteristics (e-g). (e) Power spectra obtained from four strips located within the mid-plane of the 6.5-nm bands. (f) Power spectra obtained from five strips located within the central 4.5-nm band. (g) Power spectra obtained from four strips located within the high-intensity (dark) headgroup bands. The 4.5-nm-thick band, including its mid-plane, and the headgroup bands are thus amorphous but have, at the same time, some intrinsic order with recurring characteristics of low reproducibility (f, g). The mid-plane low-intensity region of the 6.5-nm-thick bands is amorphous (e). In (d-g) the extracted power spectra are connected to their respective sampling locations (two-pixel-wide strips) in the CEMOVIS micrograph (c). Pixel size in (b, c): 3.31 Å.

6.5-nm distance is consistent with two apposing C24 amide-bound fatty acid chains plus one CER headgroup ( $48\text{C} \times 1.27\text{ \AA} + 5.1\text{ \AA} = 66\text{ \AA}$ ; C24 fatty acids dominate in stratum corneum (Masukawa *et al.*, 2009)). The 4.5-nm distance is consistent with two apposing C18 sphingoid backbone chains plus one CER headgroup ( $36\text{C} \times 1.27\text{ \AA} + 5.1\text{ \AA} = 51\text{ \AA}$ ; C18 sphingoid backbones dominate in stratum corneum (Masukawa *et al.*, 2009)).

The proposed lipid organization is optimal in terms of packing, with the fatty acid chain lengths matching the CER fatty acid chains and CHOL matching the CER sphingoid chains. This “hydrophobic matching” minimizes the potential energy of the molecular configuration. The “segregation” of CHOL and FFAs to the respective ends of the CERs may be expected, as CHOL and stratum corneum FFAs do not mix in model systems (Norlén *et al.*, 2007). CHOL, however, does

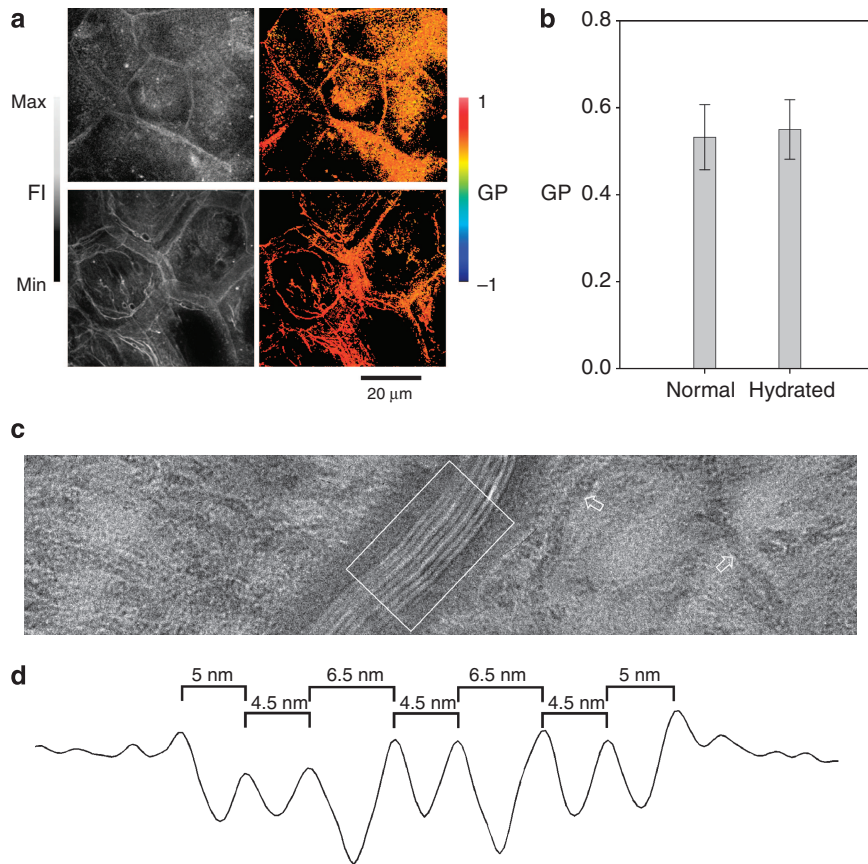


**Figure 4. The stratum corneum lipid matrix is in a condensed state and remains unaltered upon hydration.** (a) 6-Dodecanoyl-2-dimethylaminonaphthalene (LAURDAN) fluorescence intensity (left) and LAURDAN generalized polarization (GP) function images (right) of normal near-native skin (top panel) and of skin exposed to hydration for 2 hours *in vivo* (bottom panel). The images were obtained at the level of mid-part of the stratum corneum using a multi-photon excitation microscope. (b) Bar graphs (average  $\pm$  SD) showing the LAURDAN GP values of normal and hydrated skin. The high ( $>0.5$ ) LAURDAN GP values show that the extracellular lipid matrix is in a condensed state and displays little, if any, water dipolar relaxation at the lipid headgroup interface regions. (c) High-magnification cryo-electron microscopy of vitreous skin section (CEMOVIS) micrograph of the extracellular space in the mid-part of the stratum corneum after hydration. (d) Intensity profile obtained from fuzzy distance-based path growing of the area marked by a white box in (c). Note that the intensity profile after skin hydration (d) is identical to that of normal skin (compare Figure 1e). Also note the loose arrangement of keratin intermediate filaments (open arrows) in the swollen stratum corneum cells as compared with their condensed arrangement in normal stratum corneum (compare Figure 1a). The CEMOVIS intensity profile of the extracellular lipid matrix thus remains unaltered on hydration. Pixel size in (c): 3.31 Å.

mix with sphingosine and its derivatives (Garmy *et al.*, 2005). The hydrophobic match between CHOL and saturated alkyl chains is optimized between 14 and 18C chain lengths, which correspond to the length of the CHOL molecule (Ouimet and Lafleur, 2004). Further, wide-angle X-ray diffraction experiments on isolated stratum corneum indicate crystalline-like hydrocarbon chain packing with characteristic distances of 3.7–3.8 Å and 4.1–4.2 Å (Wilkes *et al.*, 1973; White *et al.*, 1988; Garson *et al.*, 1991; Bouwstra *et al.*, 1992; Hatta *et al.*, 2006), which would not appear if CHOL were distributed throughout both lipid hydrocarbon chains of the CERs. However, a stratum corneum lipid matrix in which CHOL and FFAs are segregated into different bands does allow for crystalline-like hydrocarbon chain packing on the fatty acid sides of the stacked extended CER bilayer system. It thus rationalizes how a biological lipid system composed of 30% CHOL could express crystalline-like wide-angle X-ray diffraction patterns without signs of lateral crystal domain formation detectable by high-resolution CEMOVIS.

The power spectra obtained along the lamellar plane reflect the lateral lipid packing at a resolution of 1–2 nm, which characterizes our CEMOVIS micrographs. The following comments therefore refer to the microstructure rather than the molecular-level packing of headgroups or alkyl chains. Overall, the microstructure is predominantly disordered, but there are some recurring characteristics detectable in the power spectra (Figure 3). These characteristics were most evident around the mid-plane of the 6.5-nm bands, i.e., the CER fatty acid moiety region, and corresponded to periodicities of 2.3–3.0 nm and 1.5–1.7 nm (Figure 3d). They correspond roughly to the distance between (2–4 nm) and width of (1–1.5 nm) the “cross stripes” observed within the 6.5-nm bands of the CEMOVIS micrographs (Figure 1d, open white arrows). These periodicities may therefore reflect the average repeat distance and width of coherent lipid clusters separated by defect regions. Remarkably, the perpendicular cross-stripe pattern could be recreated in the simulated electron micrographs by randomly rotating

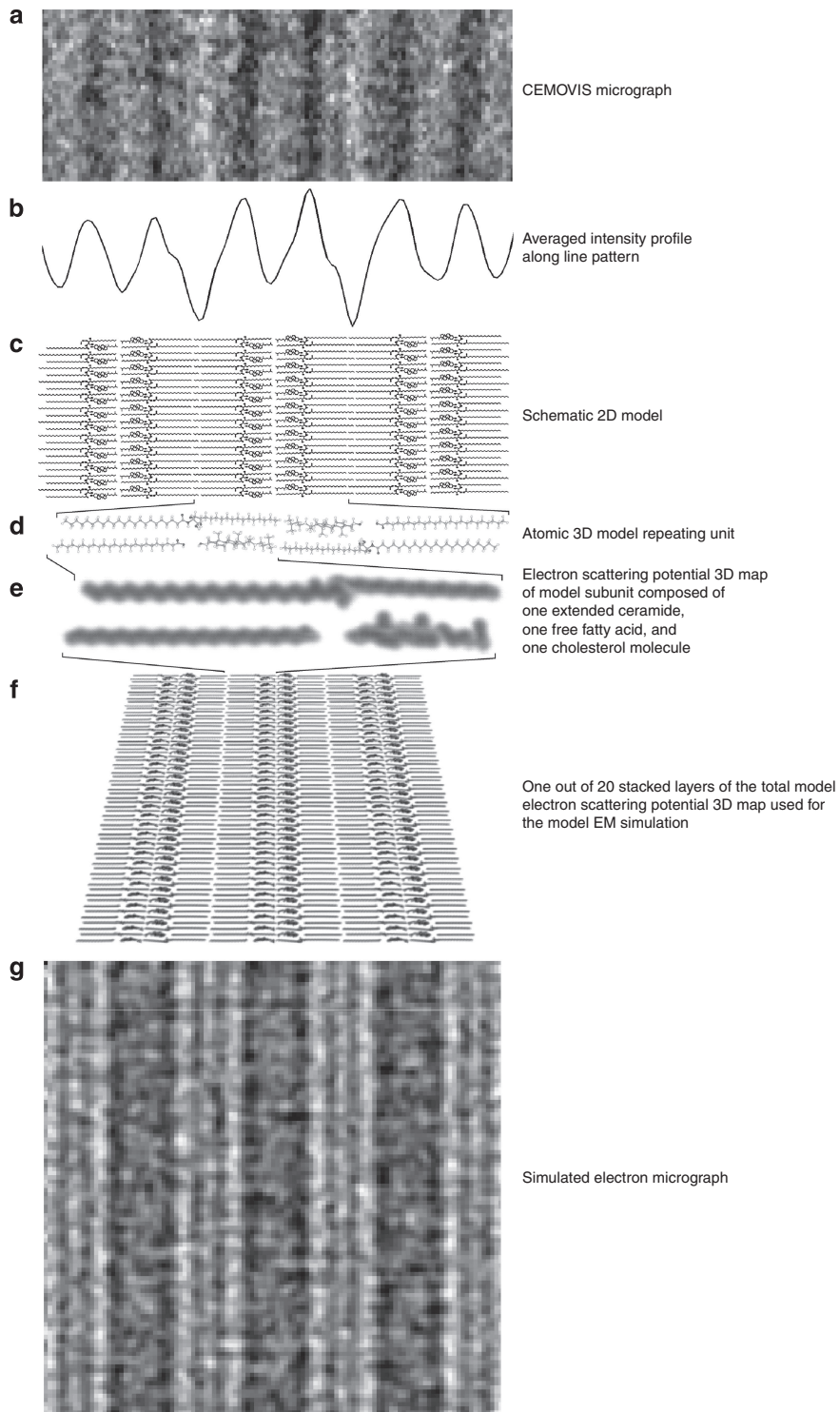


**Figure 5. Electron microscopy (EM) simulation of the stratum corneum extracellular lipid matrix.** (a) High-magnification cryo-electron microscopy of vitreous skin section (CEMOVIS) micrograph of the extracellular space in the mid-part of the stratum corneum. (b) Corresponding intensity profile obtained by fuzzy distance-based path growing (compare Figure 1b and c). (c) Schematic two-dimensional (2D) illustration of ceramides (CERs) (tetracosanylphytosphingosine (C24:0)) in fully extended conformation with cholesterol (CHOL) associated with the CER sphingoid part, and free fatty acids (FFAs) (lignoceric acid (C24:0)) associated with the CER fatty acid part. (d) Atomic three-dimensional (3D) model of the repeating unit composed of two mirrored subunits, each composed of one fully extended CER, one CHOL, and one FFA molecule. (e) Calculated electron scattering potential of one model subunit. (f) Calculated electron scattering potential 3D map of the topmost layer out of 20 superimposed layers used to generate the simulated electron micrograph (g). Defocus (a, g):  $-2.5\text{ }\mu\text{m}$ . Pixel size in (a, g):  $3.31\text{ \AA}$ .

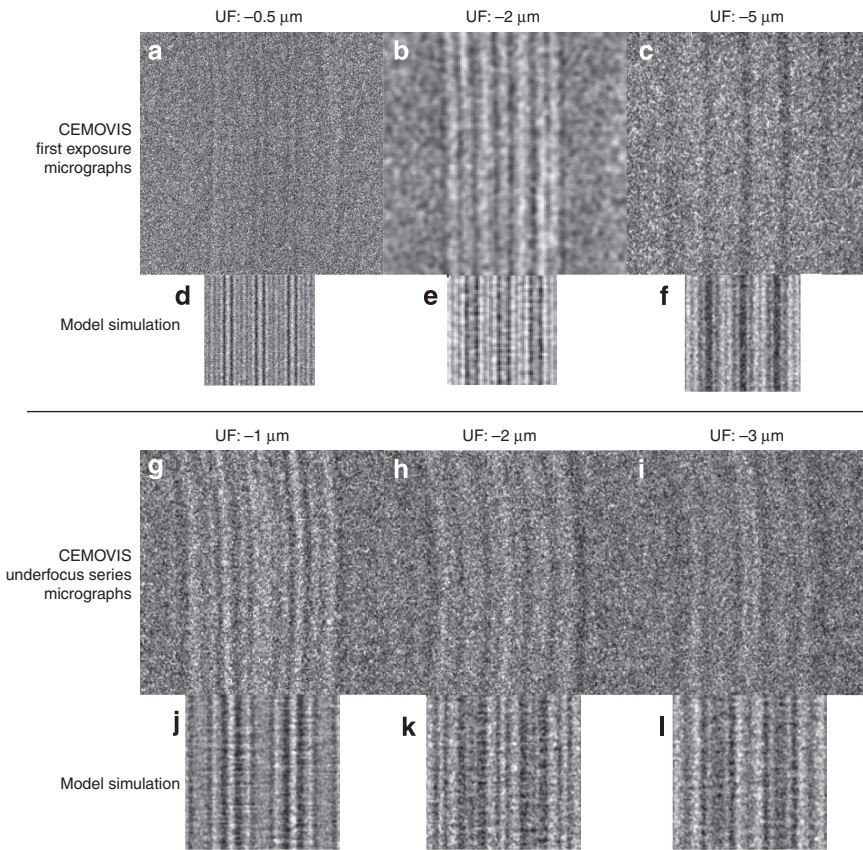


**Figure 6. Electron microscopy (EM) simulation of alternating fully extended ceramides (CERs) with selective localization of cholesterol to the CER sphingoid part accurately accounts for the observed cryo-electron microscopy of vitreous skin section (CEMOVIS) intensity pattern, as well as for the interference pattern changes observed in sequential CEMOVIS micrograph defocus series obtained at very high magnification ( $\leq 1.88 \text{ \AA}$  pixel size).**

(a-c) High-magnification CEMOVIS micrographs (first-exposure images) of the extracellular space in the mid-part of the stratum corneum obtained at (a)  $-0.5 \mu\text{m}$ , (b)  $-2 \mu\text{m}$ , and (c)  $-5 \mu\text{m}$  defocus. At very low defocuses ( $-0.5 \mu\text{m}$ ) (a) CEMOVIS intensity patterns can only be observed at very high magnification ( $\leq 1.88 \text{ \AA}$  pixel size). At very high defocuses ( $-5 \mu\text{m}$ ) (c) image resolution is low but still allows for resolution of the  $\sim 11\text{-nm}$  repeating unit. The slightly larger lamellar repeat distance in (b) ( $\sim 12 \text{ nm}$ ) compared with (a) and (c) ( $\sim 11 \text{ nm}$ ) may be due to more pronounced compression of the vitreous skin section during cryo-sectioning along the lamellar plane in (b) compared with that in (a) and (c). (d-f) represents corresponding atomic three-dimensional (3D) model (compare Figure 5) EM simulation images recorded at (d)  $-0.5 \mu\text{m}$ , (e)  $-2 \mu\text{m}$ , and (f)  $-5 \mu\text{m}$  defocus. (g-i) Sequential CEMOVIS micrograph defocus series obtained at very high magnification ( $1.88 \text{ \AA}$  pixel size) at (g)  $-1 \mu\text{m}$ , (h)  $-2 \mu\text{m}$ , and (i)  $-3 \mu\text{m}$  defocus. Note the fine changes in interference patterns caused by gradually increasing the microscope's defocus during repeated image acquisition at a fixed position. Owing to electron beam damage after repeated electron exposure, the image contrast is lower in micrographs (h, i) compared with micrograph (g), which was acquired first. In micrograph (i), some shrinkage can be observed. This is probably due to mass loss during repeated electron exposure. In addition, the curvature of the lamellar pattern is slightly increased in micrographs (h, i) compared with that in micrograph (g), which may similarly be caused by nonhomogeneous mass loss during repeated electron exposure. (j-l) Represents corresponding atomic 3D model (compare Figure 5) EM simulation images recorded at (j)  $-1 \mu\text{m}$ , (k)  $-2 \mu\text{m}$ , and (l)  $-3 \mu\text{m}$  defocus. It is shown that the atomic 3D model in Figure 5 accurately accounts not only for the major features of the CEMOVIS micrographs (a-f) but also for the interference intensity pattern changes observed upon varying the microscope's defocus during image acquisition at very high magnification (g-l). UF, under focus. Pixel size in (c, f):  $3.31 \text{ \AA}$ , in (b, e):  $6.02 \text{ \AA}$ , and in (a, d and g-l):  $1.88 \text{ \AA}$ .

the individual lipid molecules along their length axes and displacing them  $\pm 1 \text{ \AA}$  in the x, y, and z directions (Figure 5g).

A particularly notable feature of the proposed lipid structure is that it comprises a bilayer rather than an arrangement of stacked monolayers. Energetically, either arrangement should be feasible, given that leaflets of extended CER structures present alkyl chains at both ends, and therefore both organizations exclusively involve hydrocarbon interactions between leaflets. The preference for the bilayer organization in the stratum corneum lipid matrix could result

from the biological processes involved in its formation. The lipid matrix is formed from stacked bilayers of glycosylceramides in the hairpin conformation in a hydrated environment, after deglycosylation and dehydration (Holleran *et al.*, 1993; Caspers *et al.*, 2001; Norlén, 2001; Al-Amoudi *et al.*, 2005). During its formation, the extended CER bilayer organization will therefore require a transformation from hairpin to splayed chain conformation, involving a flip of one of the two CER alkyl chains. For glycosylceramides, which bind 5–10 water molecules per lipid molecule (Bach *et al.*, 1982; Bach and Miller, 1998), flip-flop is slow (half-time of

hours (Buton *et al.*, 2002)). For CERs, which only bind 0–1 water molecules per lipid molecule (Faure *et al.*, 1998), the flip-flop movement is considerably faster (half-time <1 minute (López-Montero *et al.*, 2005)). For CHOL, flip-flop is rapid (half-time <1 second (Steck *et al.*, 2002)). The initial hairpin glycosylceramide bilayer organization may therefore carry over into the extended CER bilayer organization by a flip of one of the two CER alkyl chains together with CHOL. The driving force could be the deglycosylation and dehydration encountered during the formation process. Once the strongly hydrated glycosyl groups of the glycosylceramides have been removed (Holleran *et al.*, 1993) and the water evacuated from the extracellular space (Al-Amoudi *et al.*, 2005), the extension of the two hydrocarbon chains in opposite directions aids the separation of both the ill-matched CHOL and FFAs (Norlén *et al.*, 2007), and the ill-matching CER C24 fatty acid and C18 sphingoid moieties, into different bands within an optimally close-packed stratum corneum bilayer structure. Speculatively, being a rapid membrane flipper, CHOL may facilitate the extension of the CERs by dragging the sphingoid moiety with it during the lipid matrix' reorganization from a hairpin to an extended bilayer structure.

The major physiological consequence of a condensed, fully extended CER bilayer organization is that the lipid matrix will be largely impermeable to water, as well as to both hydrophilic and lipophilic substances, because of the condensed structure and the presence of alternating lipophilic (alkyl chain) and hydrophilic (headgroup) regions (compare Figure 5c). It will be resistant toward both hydration and dehydration because of the absence of exchangeable water between lipid leaflets (compare Figure 4). Further, the proposed structure accounts for stratum corneum cell cohesion without advocating desmosomal cell-adhesion structures, and hence allows for the possibility of sliding of stratum corneum cells to accommodate skin bending. Finally, as the interaction between the individual layers of the lipid structure involves only hydrocarbons, the individual layers are relatively free to slide with respect to each other, making the matrix pliable. The lipid matrix thus meets the barrier needs of skin by being simultaneously robust and impermeable.

How does our CEMOVIS data reconcile with earlier studies? The ~11-nm repeating unit fits with the 12- to 13-nm repeating unit observed in small-angle X-ray diffraction by White *et al.* (1988), Bouwstra *et al.* (1991), Hou *et al.* (1991), and Schreiner *et al.* (2000) in isolated mouse and human stratum corneum, as well as with the 13-nm repeating unit observed by Madison *et al.* (1987) and Hou *et al.* (1991) in ruthenium tetroxide-stained mouse skin, given a preparation (dehydration)-induced slight straightening of lipid alkyl chains in these studies. Further, in ruthenium tetroxide-stained stratum corneum (compare Supplementary Figure S9A online), the electron intensity pattern of the extracellular lipid matrix expresses a broad:narrow:broad electron lucent band pattern (Madison *et al.*, 1987), which is consistent with our data given that ruthenium tetroxide not only associates with lipid headgroups but also penetrates to some extent between the lipid leaflets when facilitated by local liquid-like disordering

(Supplementary Figure S9C online). In the CEMOVIS micrographs, we observed a mid-plane low-intensity region in the 6.5-nm bands but not in the 4.5-nm bands (Figure 1b and d; Supplementary Figure S4A, B online). This translates to an increasingly lower atomic density toward the distal parts of the CER fatty acid and FFA alkyl chains, which would suggest a liquid-like disordered region close to terminal methyl groups. This is further supported by molecular dynamic simulations, which point at a skin lipid hydrocarbon chain arrangement involving a gradual change between condensed and liquid along the chain axes (Das *et al.*, 2009).

We are unable to comment on previous wide-angle X-ray diffraction and attenuated total reflection-Fourier transform infrared spectroscopy studies (Bouwstra *et al.*, 1992; Damien and Boncheva, 2010), particularly with respect to alkyl chain packing as to whether it is hexagonal or orthorhombic or both, as the CEMOVIS data are limited to a resolution of around 1–2 nm.

To summarize, the stratum corneum lipid matrix is, according to our analysis, organized as stacked bilayers of fully extended CERs with CHOL molecules associated with the CER sphingoid moiety. Further, despite its crystalline-like character, it is malleable. This condensed but pliable fully extended CER bilayer organization with asymmetric CHOL distribution rationalizes the skin's low permeability toward water and toward hydrophilic and lipophilic substances, as well as the skin barrier's robustness toward hydration and dehydration, environmental temperature and pressure changes, stretching, compression, bending, and shearing.

#### Final remarks

Until now, progress in skin barrier replacement, skin barrier repair, skin permeability enhancement, and skin protection has largely resulted from empirical efforts, treating the stratum corneum lipid matrix as a black box. The molecular description of the lipid matrix presented here may constitute a molecular platform for the above research goals, and in particular for *in silico* approaches such as molecular simulations, as well as for *in vitro* modeling, to underpin interactions of the lipid matrix with drugs and other chemicals. For example, it is foreseeable that this knowledge of the lipid organization will now enable *in silico* screening to identify molecules for enhancing skin penetration for drug delivery and to find "tightening" or "repair" molecules for the stratum corneum lipid matrix. Further, it may constitute a reference for engineering artificial skin for the treatment of wounds and burn injuries.

More generally, the novel methodological approach we have used, that combines very high magnification CEMOVIS defocus series with molecular modeling and EM simulation, may open the way for determining the near-native molecular organization of other structures in normal and diseased cells and tissues.

#### MATERIALS AND METHODS

A more detailed description of experimental procedures is available in Supplementary Information.

Skin biopsy specimens were collected from the human volar forearm and abdomen of five Caucasian males in their 40s–50s with no history of skin disease. The samples were immediately vitrified using a Leica EMPACT2 high-pressure freezer and cryosectioned at  $-140^{\circ}\text{C}$ . Images were recorded at  $-0.5$  to  $-5\text{ }\mu\text{m}$  defocus, at  $120\text{ kV}$ , at a dose of  $1,000$ – $17,000$  electrons  $\text{nm}^{-2}$  per image and a pixel size of  $6.02$ ,  $3.31$ , and  $1.88\text{ \AA}$ , respectively, in a FEG CM200 FEI microscope equipped with a cooled slow-scan  $2048 \times 2048$  TVIPS TemCam-F224 HD CCD camera.

The averaged intensity profiles of the cryo-electron micrographs were obtained by fuzzy distance-based image analysis. A path was automatically extracted based on the shortest intensity-weighted distance between two points. Along the path, perpendicular intensity profiles were extracted (Figure 1c) and then averaged (Figure 1e).

To accurately estimate the distance between intensity peaks, numerical analysis was used, based on least-squares fitting between the central part of the measured intensity peaks and a Gaussian model (Supplementary Figure S3 online).

To check the degree of the packing order of the  $6.5$ - and  $4.5\text{-nm}$  bands, power spectra of 2-pixel-wide strips parallel to the bands in the micrographs were extracted (Figure 3).

To evaluate the native phase state and the hydration behaviour of the stratum corneum lipid matrix, multi-photon excitation microscopy LAURDAN GP measurements were performed on excised forearm skin before and after hydration *in vivo* (Figure 4a and b).

Simulated CEMOVIS images for the different atomic models (Supplementary Figures S6D3–J5, S7D3–J5, and S8D3–E5) were created with a computer program simulating the interaction between the potential map and the electron beam, the optical transformation effect of the lens system of the microscope, and the image formation on the detector (Rullgård *et al.*, 2011). The software is freely available at <http://tem-simulator.sourceforge.net/>.

#### CONFLICT OF INTEREST

The authors state no conflict of interest.

#### ACKNOWLEDGMENTS

We thank Bertil Daneholt for unwavering support and encouragement for more than a decade. We also thank Ozan Öktem, Jacques Dubochet, Massimo Noro, Chinmay Das, Emma Sparre, Johan Engblom, Philip Wertz, Ichiro Hatta, Jonathan Hadgraft, Richard Guy, Marek Haftek, Richard Mendelsohn, Stephen Hoath, David Moore, Jennifer Thewalt, Walter Holleran, Gopi Menon, Michael Roberts, Fred Frasch, Gabriel Wittum, Jim Riviere, Samir Mitragotri, Jesus Perez Gil, Thomas McIntosh, Reinhard Neubert, and our reviewers for invaluable comments on the manuscript. The present work was made possible by the generous support from the Swedish Medical Society, Swedish Research Council, Oriflame, Shiseido Japan, LEO Pharma, Wenner-Gren foundation, Welander Foundation, European community (3D-EM Network of Excellence), Visualization Program by Knowledge Foundation, Vårdal Foundation, Foundation for Strategic Research, VINNOVA, Invest in Sweden Agency, Forskningsrådet for Sundhed og Sygdom (FSS, Denmark), and the Danish National Research Foundation. The Knut and Alice Wallenberg Foundation is acknowledged for support of the electron microscope facility. II developed and performed high-resolution (pixelsize  $\leq 3.31\text{ \AA}$ ; nominal section thickness  $20$ – $30\text{ nm}$ ) CEMOVIS and designed the *in vivo* hydration/dehydration experiment. HH and LdH performed CEMOVIS. SS developed the fuzzy distance-based analysis method. L-GÖ performed the EM model simulations. JA constructed the atomic three-dimensional models, formulated the alternative models with LN, and contributed to the writing of the paper. JB, MB, and LAB performed the multi-photon excitation microscopy LAURDAN GP analysis. AL and DN assisted the CEMOVIS data analysis. SM supported the high-resolution CEMOVIS development and data collection. US performed the numerical curve fitting analysis and the power spectra analysis. LN designed the study, analyzed the data, formulated the model, and wrote the paper.

#### SUPPLEMENTARY MATERIAL

Supplementary material is linked to the online version of the paper at <http://www.nature.com/jid>

#### REFERENCES

- Al-Amouri A, Chang JJ, Leforestier A *et al.* (2004) Cryo-electron microscopy of vitreous sections. *EMBO J* 23:3583–8
- Al-Amouri A, grave;ez DC, Betts MJ *et al.* (2007) The molecular architecture of cadherins in native epidermal desmosomes. *Nature* 450: 832–837
- Al-Amouri A, Dubochet J, Norlén L (2005) Nanostructure of the epidermal extracellular space as observed by cryo-electron microscopy of vitreous sections of human skin. *J Invest Dermatol* 124:764–77
- Bach D, Miller IR (1998) Hydration of phospholipid bilayers in the presence and absence of cholesterol. *Biochim Biophys Acta* 1368: 216–24
- Bach D, Sela B, Miller IR (1982) Compositional aspects of lipid hydration. *Chem Phys Lipids* 31:381–94
- Bouwstra JA, Gooris GS, Van der Spek JA *et al.* (1991) Structural investigations of human stratum corneum by small-angle X-ray scattering. *J Invest Dermatol* 97:1005–12
- Bouwstra JA, Gooris GS, Salmon-de Vries MA *et al.* (1992) Structure of human stratum corneum as a function of temperature and hydration: a wide-angle x-ray diffraction study. *Inter J Pharmaceut* 84:205–16
- Breathnach AS, Goodman T, Stolinski C *et al.* (1973) Freeze fracture replication of cells of stratum corneum of human epidermis. *J Anat* 114:65–81
- Buton X, Hervé P, Kubelt J *et al.* (2002) Transbilayer movement of monohexosylphingolipids in endoplasmatic reticulum and Golgi membranes. *Biochemistry* 41:13106–15
- Caspers PJ, Lucassen GW, Carter EA *et al.* (2001) *In vivo* confocal raman microspectroscopy of the skin: noninvasive determination of molecular concentration profiles. *J Invest Dermatol* 116:434–42
- Damien F, Boncheva M (2010) The extent of orthorhombic lipid phases in the stratum corneum determines the barrier efficiency of human skin *in-vivo*. *J Invest Dermatol* 130:611–4
- Das C, Olmsted PD, Noro M (2009) Simulation studies of stratum corneum lipid mixtures. *Biophys J* 97:1941–51
- Dubochet J, Adrian M, Chang JJ *et al.* (1988) Cryo electron microscopy of vitrified specimens. *Q Rev Biophys* 21:129–228
- Elias PM, Friend DS (1975) The permeability barrier in mammalian epidermis. *J Cell Biol* 65:180–91
- Fanelli D, Öktem O (2008) Electron tomography: a short review with an emphasis on the absorption potential model for the forward problem. *Inverse Probl* 24:013001 (51pp)
- Faure C, Tranchant J-F, Duforc EJ (1998) Interfacial hydration of ceramide in stratum corneum model membrane measured by  $^{2}\text{H-NMR}$  of  $\text{D}_2\text{O}$ . *J Chim Phys* 95:480–6
- Garmy N, Taieb N, yahi N *et al.* (2005) Interaction of cholesterol with sphingosine: physicochemical characterization and impact on intestinal absorption. *J Lipid Res* 46:36–45
- Garson JC, Doucet J, Leveque J-L *et al.* (1991) Oriented structure in human stratum corneum revealed by X-ray diffraction. *J Invest Dermatol* 96:43–49
- Hatta I, Ohta N, Inoue K *et al.* (2006) Coexistence of two domains in intercellular lipid matrix of stratum corneum. *Biochim Biophys Acta* 1758:1830–6
- Holleran WM, Takagi Y, Menon G *et al.* (1993) Processing of epidermal glycosylceramides is required for optimal mammalian cutaneous permeability barrier function. *J Clin Invest* 91:1656–64
- Hou SYE, Mitra AK, White SH *et al.* (1991) Membrane structures in normal and essential fatty acid-deficient stratum corneum: characterization by ruthenium tetroxide staining and X-ray diffraction. *J Invest Dermatol* 96:215–23
- López-Montero I, Rodriguez N, Cribier S *et al.* (2005) Rapid transbilayer movement of ceramides in phospholipids vesicles and in human erythrocytes. *J Biol Chem* 280:25811–9

- Madison KC, Swartzendruber DC, Wertz PW et al. (1987) Presence of intact intercellular lamellae in the upper layers of the stratum corneum. *J Invest Dermatol* 88:714–8
- Masukawa Y, Narita H, Sato H et al. (2009) Comprehensive quantification of ceramide species in human stratum corneum. *J Lipid Res* 50: 1708–19
- McIntosh TJ (2003) Organization of skin stratum corneum extracellular lamellae: diffraction evidence for asymmetric distribution of cholesterol. *Biophys J* 85:1675–81
- Norlén L (2001) Skin barrier formation: the membrane folding model. *J Invest Dermatol* 117:823–9
- Norlén L, Öktem O, Skoglund U (2009) Molecular cryo-electron tomography of vitreous tissue sections: current challenges. *J Microsc* 235: 293–307
- Norlén L, Plasencia I, Simonsen A et al. (2007) Human stratum corneum lipid organization as observed by atomic force microscopy on Langmuir–Blodgett films. *J Struct Biol* 158:386–400
- Quimet J, Lafleur M (2004) Hydrophobic match between cholesterol and saturated fatty acid is required for the formation of lamellar liquid ordered phases. *Langmuir* 20:7474–81
- Rullgård H, Öfverstedt L-G, Masich S et al. (2011) Simulation of transmission electron microscope images of biological specimens. *J Microsc* 243: 234–56
- Schreiner V, Gooris GS, Pfeiffer S et al. (2000) Barrier characteristics of different human skin types investigated with X-ray diffraction, lipid analysis, and electron microscopy imaging. *J Invest Dermatol* 114: 654–60
- Steck TL, Ye J, Lange Y (2002) Probing red cell membrane cholesterol movement with cyclodextrine. *Biophys J* 83:2118–25
- Wertz P, Norlén L (2003) “Confidence Intervals” for the “true” lipid compositions of the human skin barrier?. In: Forslind B, Lindberg M (eds) *Skin, Hair, and Nails Structure and Function*. Marcel Dekker, New York, pp 85–106
- White SH, Mirejovsky D, King GI (1988) Structure of lamellar lipid domains and corneocyte envelopes of murine stratum corneum. An x-ray diffraction study. *Biochemistry* 27:3725–32
- Wilkes GL, Nguyen AL, Wildnauer R (1973) Structure-property relations of human and neonatal rat stratum corneum. I. Thermal stability of the crystalline lipid structure as studied by X-ray diffraction and differential thermal analysis. *Biochim Biophys Acta* 304:265–75



This work is licensed under the Creative Commons Attribution-NonCommercial-No Derivative Works 3.0 Unported License. To view a copy of this license, visit <http://creativecommons.org/licenses/by-nc-nd/3.0/>